ELSEVIER

Journal of Neuroscience Methods 161 (2007) 166–182

JOURNAL OF NEUROSCIENCE METHODS

www.elsevier.com/locate/jneumeth

Exploration of event-induced EEG phase synchronization patterns in cognitive tasks using a time–frequency-topography visualization system

Alfonso Alba [a,c,*], Jose L. Marroquin [a], Joaquin Peña [a], Thalia Harmony [b], Berta Gonzalez-Frankenberger [b]

[a] *Centro de Investigation en Matematicas (CIMAT), Guanajuato, Mexico*
[b] *Instituto de Neurobiologia, UNAM Campus Juriquilla, Queretaro, Mexico*
[c] *Facultad de Ciencias, UASLP, San Luis Potosi, Mexico*

Received 3 August 2006; received in revised form 16 October 2006; accepted 25 October 2006

Abstract

In this paper, we present a method for the study of synchronization patterns measured from EEG scalp potentials in psychophysiological experiments. This method is based on various techniques: a time–frequency decomposition using sinusoidal filters which improve phase accuracy for low frequencies, a Bayesian approach for the estimation of significant synchrony changes, and a time–frequency-topography visualization technique which allows for easy exploration and provides detailed insights of a particular experiment. Particularly, we focus on in-phase synchrony using an instantaneous phase-lock measure. We also discuss some of the most common methods in the literature, focusing on their relevance to long-range synchrony analysis; this discussion includes a comparison among various synchrony measures. Finally, we present the analysis of a figure categorization experiment to illustrate our method.

Keywords: EEG; Phase synchronization; Time–frequency-topography; Sinusoidal filters; Markov random field; Bayesian classification

1. Introduction

In recent years, there has been an increasing interest in EEG related to patterns of synchronization and desynchronization that are observed in the electrophysiological activity of the brain. Interest in these phenomena has developed as a result of the view that they might provide a window on the dynamics of cell assembly formation, by which spatially distributed brain areas become linked together in dynamic networks involved in sensory integration, object representation, and memory encoding or retrieval (Kirschfeld, 2005; Bastiaansen and Hagoort, 2003).

Oscillations in the EEG indicate periodic activity of large populations of synchronized neurons which are usually called neuronal assemblies, a term coined by Hebb (1949). The formation of such assemblies is observed in various sensory, behavioral or cognitive states. Several kinds of events, the most notably being sensory stimuli, produce two different types of EEG changes: "evoked" activities which are exactly time-locked and phase-locked to the stimulus, and "induced" activities which are changes in the EEG that are only approximately time-locked, but not phase-locked (Pfurtscheller and Lopes da Silva, 1999), and thus cannot be extracted by a simple linear method such as averaging, but may be detected by frequency analysis. Induced activity is thought to reflect functional changes in the parameters controlling dynamic interactions within and between brain structures. This means that these induced-related phenomena represent frequency specific changes of the ongoing EEG activity, and may consist, in general terms, either on increases or decreases of power in specific regions of the time–frequency (TF) plane. This may be considered to be due to an increase or a decrease in synchrony of the underlying neuronal populations, respectively (Pfurtscheller, 1977, 1992), and thus are accordingly called "event-related synchronization" (ERS) and "event-related desynchronization" (ERD). These events may be characterized by specific activation patterns, which are located in particular regions of the TF plane, and which may be associated with specific cognitive sub-processes (Marroquin et al., 2004; Harmony et al., 2001).

There is, however, another important characteristic of these events, which cannot be measured directly by relative power changes: the formation of dynamic global assemblies, which

* Corresponding author at: CIMAT, Apartado Postal 402, Guanajuato, Gto. 36240, Mexico. Tel.: +52 473 7327155x49673; fax: +52 473 7325749.
E-mail address: falbac@cimat.mx (A. Alba).

0165-0270/$ – see front matter © 2006 Elsevier B.V. All rights reserved.
doi:10.1016/j.jneumeth.2006.10.018

according to the definition by Varela et al. (2001), are "distributed local networks of neurons transiently linked by reciprocal dynamic (possibly long range) connections". It is generally accepted that these connections are correlated with the synchronization of the corresponding EEG signals in particular regions of the TF plane (Varela et al., 2001; Lopes da Silva, 1991; Singer, 1993). Also, simulations performed with neural mass models show that a bidirectional coupling of two remote cortical areas is reflected as phase synchronization of MEG/EEG oscillations (David and Friston, 2003), which supports the idea that EEG synchrony is highly related to physiological connectivity in the cortex and thus can be used as a measure for long-range interaction.

For these reasons, there have been a number of studies of long range synchronization of EEG signals (Bressler, 1995; Friston et al., 1997; Lachaux et al., 1999, 2000; Rodriguez et al., 1999). Most of these studies, however, have some limitations: on one hand, the high dimensionality of the synchrony data implies a visualization problem. Most works on the field avoid this problem by averaging across a large time window (Quian Quiroga et al., 2002; David et al., 2004; Mizuhara et al., 2005) and/or by limiting the analysis to specific frequency bands (Lachaux et al., 1999; Rodriguez et al., 1999). This is far from ideal since many synchronization patterns appear only in small regions of the TF plane and one cannot obtain, from these results, a complete overall picture of the synchronization dynamics across different frequencies, which may correspond to specific cognitive sub-processes. Another problem is related to the way in which significant synchronization changes are detected. These significant changes must be characterized by a persistent relative phase-locking (or phase scattering) between the signals that correspond to each pair of electrode locations; in other words, to estimate the degree of EEG synchronization one must determine the significance of a phase-locking measure and its consistency across a given time window. The most widely used synchrony measures, such as coherence and the *single trial phase-locking statistic* (STPLS) (Lachaux et al., 2000), attempt to measure this indirectly by computing the synchrony values over a given time interval. The problem with this approach is that, as will be shown later, these measures are strongly affected by local phase dispersion changes occurring in either one of the two signals, which may interfere with the detection of true synchronization or de-synchronization events.

In 2004, Marroquin et al. introduced an exploratory method for the study of ERS and ERD events (power changes), based on time–frequency-topography (TFT) displays which provided a detailed view of the topographical distributions of EEG dynamic power changes with respect to the pre-stimulus, across the full post-stimulus time segment, and at the same time, across all frequencies. The purpose of this work is to extend the TFT exploratory analysis in order to study long-range interactions using various synchrony measures, such as coherence and measures based on the phase difference of the signals. We improve the accuracy of the analysis in terms of the time–frequency decomposition by using sinusoidal quadrature filters (Guerrero et al., 2005) instead of the more popular Gabor filters, and focus on a phase-locking measure which is instantaneous and thus is not dominated by local phase dispersion. Time-persistence is then handled via Bayesian estimation of a hidden Markov random field (MRF) that models a label field in TF space that classifies the interactions between signal pairs as significantly higher, lower or equal to the corresponding pre-stimulus average value. We also present a TFT visualization method that permits one to obtain a full detailed overview of the dynamic synchronization patterns (SP's), which may be correlated with concurrent cognitive processes whose expression is multiplexed at different frequencies. A comparison between different synchrony measures from an interpretative point of view is also presented. Finally, the effectiveness of these techniques is illustrated with the analysis of SP's associated with a figure classification task.

2. Materials and methods

Throughout this presentation we illustrate our procedure using data from a figure classification experiment (Harmony et al., 2001) where white-line figures on a black background were presented to each subject. The subjects were instructed to press a button if the figure corresponded to an animal whose name started with a consonant, and another button if the figure did not correspond to an animal and the name of the figure started with a consonant. If the name started with a vowel, the subject was instructed not to respond. The subjects were 18 normal children (8–10 years old, 9 females), all right handed with normal neurological examination. EEG was recorded with reference to linked ears from Fp1, Fp2, F3, F4, C3, C4, P3, P4, O1, O2, F7, F8, T3, T4, T5, T6, Fz, Cz, Pz, and Oz of the 10/20 system. EOG was recorded from a supraorbital electrode and from an electrode on the external canthus of the right eye. The amplifier bandwidth was set between 0.5 and 30 Hz. EEG was sampled every 5 ms using a MEDICID 3E system and stored on a hard disk for further analysis. Sampling was done every 5 ms during a time segment from 1280 ms before the stimulus to 1500 ms after its onset. Each trial was visually edited and only those corresponding to correct responses and with no artifacts were analyzed. Subjects were seated in a comfortable chair in front of the videomonitor. Stimuli were delivered by a MINDTRACER system synchronized to the MEDICID 3E acquisition system.

We have also tested our method with other various experiments: a word categorization experiment (Harmony et al., 2001) similar to the Figures experiment (with words presented instead of figures), a working-memory task based on the Sternberg paradigm (Harmony et al., 2004), and a Go/NoGo experiment to study the inhibition of the motor response. The analysis of these experiments essentially confirms the main results described in this paper; however, for reasons of space we do not include such studies here. Details of these results can be found in (Alba et al., 2006).

2.1. Methodology

Our procedure consists of the following steps:

1. Run the EEG signals through a bank of bandpass quadrature filters and extract phase information (TF phase analysis).

2. Calculate a synchrony measure from the filtered signals.
3. Estimate the likelihoods and prior distributions for the MRF model using the synchronization values.
4. Use Bayesian estimation to find significant synchronization patterns that are persistent.
5. Display synchronization patterns as multitoposcopic graphs and time–frequency-topography (TFT) maps.

2.2. Time–frequency phase analysis

To obtain the phase information of the EEG signals, one may pass each signal through a bandpass filter at the frequency of interest. As in a previous work (Marroquin et al., 2004), we have chosen to use a bank of quadrature filters centered at each Hz and with a fixed bandwidth (about 1.76 Hz within 3 db of attenuation) to facilitate interpretation. One common choice for filters are the Gabor filters (Gabor, 1946), which provide the best balance between time and frequency localization in terms of the Heisenberg product. However, because of their Gaussian frequency response, at lower tuning frequencies Gabor filters may have a significant response to negative frequencies and lose their quadrature property, which results in distorted phase estimates (see Fig. 1a). In particular, if a unit-gain Gabor filter tuned at a frequency of h Hz has gain equal to α (with $\alpha < 1$) for the corresponding negative frequency $-h$, the argument of the complex filter output at time t corresponding to an input signal $s(t) = \cos(2\pi ht + \phi)$, where ϕ is a constant phase, will be

$$\hat{\Phi}(t) = \rho(\Phi(t)) = \arctan\left(\frac{1-\alpha}{1+\alpha}\tan\ \Phi(t)\right), \tag{1}$$

where $\Phi(t) = 2\pi ht + \phi$ is the argument of the ideal output $e^{i\Phi(t)}$ (obtained with $\alpha = 0$). The distortion signal $d(t) = \Phi(t) - \hat{\Phi}(t)$ will be zero when $\tan\Phi(t)$ equals 0 or $\pm\infty$, i.e., for $t = k/4h - \phi/2\pi h$, with $k = 0, 1, \ldots$, and will change its sign between these values, which means that it will oscillate at twice the tuning frequency h.

If $s(t)$ has a more complex structure (i.e., if it is a sum of sinusoids with different frequencies, amplitudes, and phases), this distortion cannot be characterized in an easy way, but it will have a significant effect on the measured phase.

This problem may be avoided if one uses filters that are forced to have zero gain for negative frequencies. In particular, one may use a bank of sinusoidal quadrature filters (SQF's) (Guerrero et al., 2005) which have the following frequency response:

$$G_{\omega_k,h}(\omega) = \begin{cases} \frac{1}{2}\left[1 + \sin\left(\frac{(h_k+2(\omega-\omega_k))\pi}{2h_k}\right)\right], & \text{if } \omega \in [\omega_k - h_k, \omega_k], \\ \frac{1}{2}\left[1 + \sin\left(\frac{(h+2(\omega-\omega_k))\pi}{2h}\right)\right], & \text{if } \omega \in [\omega_k, \omega_k + h_k], \\ 0 & \text{otherwise,} \end{cases} \tag{2}$$

where ω_k is the center frequency for the kth filter, h is the bandwidth, and $h_k = \min\{h, \omega_k\}$. The convolution kernel $g_{\omega_k,h}$ of the SQF's is found as the inverse Fourier transform of $G_{\omega_k,h}$. These filters have a response that is almost identical to Gabor filters at tuning frequencies higher than 6 Hz; however at lower tuning frequencies, the asymmetrical response of the sinusoidal quadrature filters yields a correct phase, as shown in Fig. 1a.

To analyze the effect of this distortion on the estimated synchrony between two signals, we make the following considerations: the filtered signals $F_{j,\omega,e}$, from which one can extract the instantaneous amplitude $A_{j,\omega,e}(t)$ and the instantaneous argument $\Phi_{j,\omega,e}(t)$, are obtained by convolution with a filter kernel $k_{\omega,h}$:

$$F_{j,\omega,e}(t) = (k_{\omega,h} \times V_{j,e})(t) = A_{j,\omega,e}(t)\exp[i\Phi_{j,\omega,e}(t)]. \tag{3}$$

If the actual argument Φ of the component with frequency ω is $\Phi(t) = \omega t + \phi_{j,\omega,e}(t)$, then the estimated argument $\hat{\Phi}$ may be expressed as a function ρ of the actual argument, where ρ is given by Eq. (1).

As one can see in Fig. 1a, for SQF's ρ is linear, while for Gabor filters it is clearly not. Since most phase-synchrony measures depend on the phase difference $\Delta\hat{\Phi}(t) = \hat{\Phi}_1(t) - \hat{\Phi}_2(t) = \rho(\omega t + \phi_1(t)) - \rho(\omega t + \phi_2(t))$, it is clear that a non-linear ρ will not cancel the terms involving ωt, and will instead introduce an oscillation in $\Delta\hat{\Phi}$, even if the true phase difference $\phi_1 - \phi_2$ is held constant.

We have performed a series of tests in order to demonstrate the improvement of SQF's over Gabor filters for synchrony estimation. For these tests we applied the average magnitude of the phase difference (MPD) as synchrony measure and the Bayesian analysis described below. Using Gabor filters, the sensitivity of the synchrony measure shows a cyclic dependence on the time t, which corresponds to the distortions in the phase observed in Fig. 1a.

The simulated data used for the tests is obtained from a very simple model which consists of a 2 Hz sinusoidal plus noise. The signals are given by:

$$V_{j,e} = \cos(2\pi f_0 t + \phi_{j,e}) + R_{j,e}(r,t), \quad \phi_{j,e} \sim \mathcal{N}(0,\sigma), \tag{4}$$

where j is the trial number, e the electrode index, $f_0 = 2$ Hz is the frequency of the sinusoidal, and σ is the standard deviation of the distribution of the phases, which controls the degree of synchrony between the signals (lower values of σ imply higher synchrony). The noise function $R_{j,e}(r,t)$ depends on the "noise level" r. For our tests, we used two electrodes ($e = 1, 2$), $\sigma_{\text{pre}} = \pi/10$ (pre-stimulus σ), and $\sigma_{\text{post}} = \pi/20$ (post-stimulus σ). Since $\sigma_{\text{pre}} > \sigma_{\text{post}}$, we are thus modeling an increase of synchrony in the full post-stimulus segment. We have generated 20 datasets with 50 trials each. For each dataset we perform the procedure described below in order to obtain a class label field $c_{\omega,e_1,e_2}(t)$ which indicates if synchrony between e_1 and e_2 at a frequency ω is significantly higher ($c = 1$), lower ($c = -1$), or equal ($c = 0$) with respect to the pre-stimulus average. The expected class is $c(t) = 1$ for all t in the post-stimulus segment.

For the first test we used Gaussian noise given by

$$R_{j,e}(r,t) \sim \mathcal{N}(0,r). \tag{5}$$

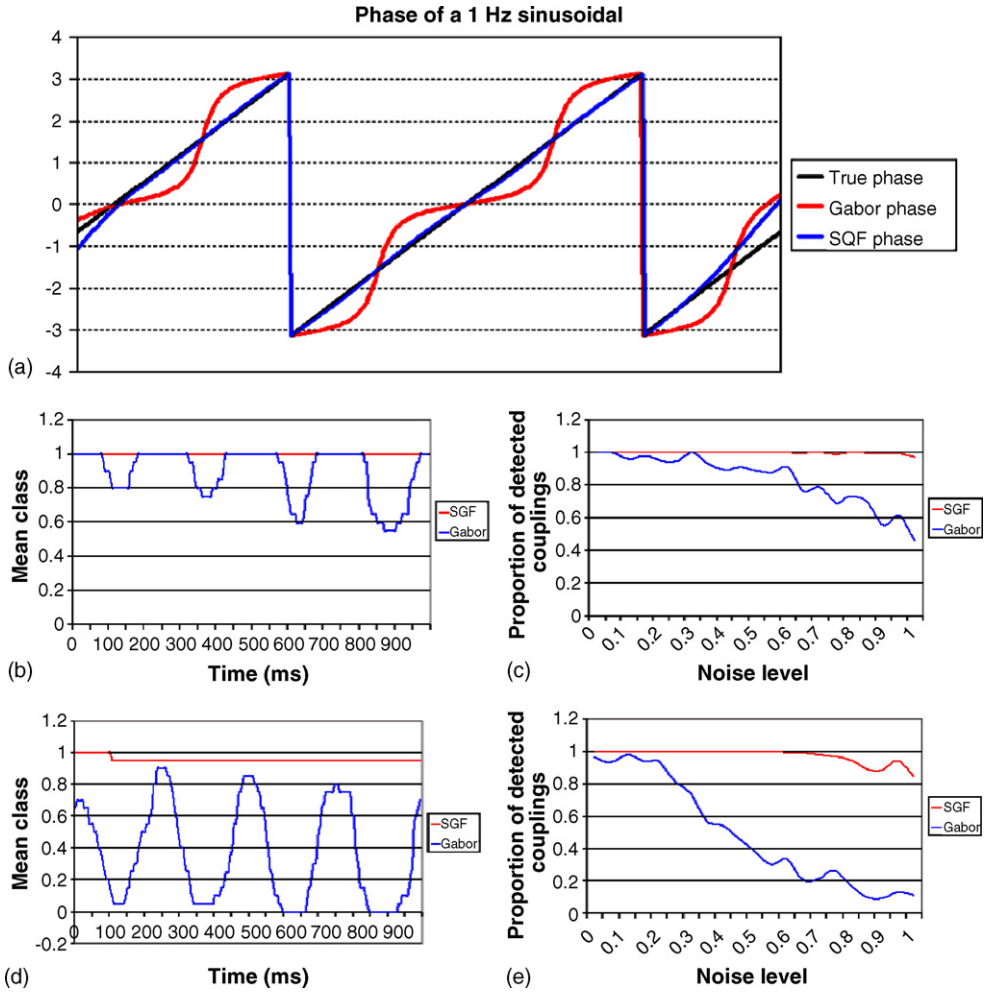

Fig. 1. Comparison between Gabor filters and SQF's. "(a) True phase and estimated phase (using Gabor and sinusoidal quadrature filters) for a 1 Hz sinusoidal input signal." (b–e) Comparison using simulated data with Gaussian noise for (b and c), and with interference of sinusoidals for (d and e). Graphs (b and d) show the average class $\bar{c}(t)$ computed across 20 datasets, whereas (c and e) show the proportion of detected couplings with respect to the noise level.

With a noise level $r = 0.5$, the average class $\bar{c}(t)$ across all datasets is shown in Fig. 1b. The blue line represents the results obtained using Gabor filters, whereas the red line corresponds to sinusoidal quadrature filters. The oscillating distortion is clearly present with the Gabor filters, and it corresponds to a frequency of 4 Hz (twice the tuning frequency, as shown above). Fig. 1c shows the proportion of detected couplings (i.e., with $c(t) = 1$) in the post-stimulus segment with respect to the noise level r (averaged across the 20 datasets). The proportion should remain close to 1; however, Gabor filters clearly start to fail with $r > 0.3$.

The second test uses a sum of interfering sine waves as noise function:

$$R_{j,e}(r,t) = \sum_{f!=f_0} \frac{a_f}{f} \cos(2\pi f t + \phi_f),$$

$$a_f \sim \mathcal{U}(0,r), \quad \phi_f \sim \mathcal{U}(0,2\pi). \tag{6}$$

The sum is taken across frequencies from 1 to 50 Hz, except the frequency of interest f_0, and the components are attenuated according to their frequency. As in the previous test, we calculated the average class $\bar{c}(t)$ and the proportion of detected couplings with respect to the noise level. The results, presented in Fig. 1d and e, show the same differences as in the previous example.

It is worth mentioning that using real EEG datasets (such as the Figures experiment signals), there are clear differences between the results obtained with SQF's and those obtained from Gabor filters in the first 6 Hz. The tests with simulated data indicate that the results with Gabor filters may not be reliable in the delta and theta bands.

2.3. Synchrony measures

In this section, we discuss the most commonly used synchrony measures in the literature (e.g. coherence and circular variance of the phase difference), and propose two phase-based measures that focus on in-phase (phase difference equal to zero) or anti-phase (phase difference equal to π) synchrony. Later, we will perform a statistical comparison of all the measures presented here, and highlight some of their strengths and weaknesses.

2.4. Magnitude of phase difference (MPD)

According to David and Friston's neural mass model, the EEG/MEG signals from two distant cortical areas will show a phase difference of 0 or π when there is a bidirectional coupling between the two areas (David and Friston, 2003). This is supported by other works such as Friston et al. (1997) and Rodriguez et al. (1999), where the distribution of the phase differences concentrates around zero during episodes of high synchrony. Moreover, according to David and Friston (2003), and Varela et al. (2001), the proportion of reciprocal connections in the brain is very high. Therefore, it makes sense to consider as synchrony criterion the following: two signals with instantaneous phases $\phi_1(t)$ and $\phi_2(t)$ are in synchrony when $\phi_1(t) \approx \phi_2(t)$ for all t in a given time interval. A straightforward instantaneous measure would be the magnitude of the phase difference $|\phi_1(t) - \phi_2(t)|$ which can be wrapped between $-\pi$ and π. This makes it easy to obtain a normalized measure based on the phase difference:

$$\mu_{j,\omega,e_1,e_2}(t) = 1 - \frac{1}{\pi}|\text{wrap}(\phi_{j,\omega,e_1}(t) - \phi_{j,\omega,e_2}(t))|, \tag{7}$$

where wrap(ϕ) returns the angle ϕ wrapped to the interval $[-\pi, \pi)$.

2.5. Cumulative probability of phase difference (CPPD)

An alternative to the MPD measure consists on estimating the probability of the phase difference being smaller (in absolute value) than some $\epsilon > 0$. This probability can be estimated across all trials for each t, ω, e_1, and e_2 as follows:

$$\mu_{\omega,e_1,e_2}(t) = \frac{1}{N_r}\sum_{j=1}^{N_r} I(|\text{wrap}(\phi_{j,\omega,e_1}(t) - \phi_{j,\omega,e_2}(t))| < \epsilon). \tag{8}$$

where $I(P)$ equals 1 if P is true, and zero otherwise.

This measure allows a quantification of the degree of synchrony (by means of ϵ), regardless of any further transformation applied to the measure (such as the significance analysis we perform). We have used $\epsilon = \pi/5$ rad for our tests (equivalent to 10 ms at 10 Hz).

One can modify this measure to detect anti-phase synchrony (couplings which show a phase difference of π). A simple example is given by:

$$\mu_{\omega,e_1,e_2}(t) = \frac{1}{N_r}\sum_{j=1}^{N_r} I(|\text{wrap}(\phi_{j,\omega,e_1}(t) - \phi_{j,\omega,e_2}(t) - \pi)| < \epsilon). \tag{9}$$

However, one must be careful not to confuse a decrease in synchrony with anti-phase couplings. This can be done either by using small values for ϵ, or by comparing both phase and anti-phase measures. Our tests show that only a very small number of detected couplings correspond to anti-phase synchrony.

2.6. Phase-locking statistic (PLS)

Lachaux et al. proposed as synchrony measure one minus the circular variance (see Fisher, 1995) of phase differences across trials at instant t and called it *phase-locking statistic* (PLS) (Lachaux et al., 1999):

$$\mu_{\omega,e_1,e_2}(t) = \left|\frac{1}{N_r}\sum_{j=1}^{N_r} \exp[\text{i}(\phi_{j,\omega,e_1}(t) - \phi_{j,\omega,e_2}(t))]\right|, \tag{10}$$

where N_r is the number of trials in the EEG experiment.

2.7. Single-trial phase-locking statistic (STPLS)

In order to obtain a phase-locking measure for single trials, Lachaux et al. (2000) proposed a new measure based on the variance of the phase difference across a time window centered at time t, for each trial j:

$$\mu_{j,\omega,e_1,e_2}(t) = \left|\frac{1}{2w+1}\sum_{t'=t-w}^{t+w} \exp[\text{i}(\phi_{j,\omega,e_1}(t') - \phi_{j,\omega,e_2}(t'))]\right|, \tag{11}$$

This measure will be maximal when $\phi_1(t) - \phi_2(t)$ is approximately constant for all t in a given time window. According to Varela et al. (2001), most cognitive events have a typical duration of a few hundreds of milliseconds; therefore, in all our tests we have used $w = 10$ which is equivalent to a window size of 105 ms (the window size is $2w + 1$ samples).

2.8. Coherence

Statistical coherence is a measure of how closely two time series are related by a linear transformation (Gardner, 1992) and it is widely used as a measure of EEG synchrony (Bressler et al., 1993; Bressler, 1995; Nunez, 1995; Nunez et al., 1997; Gross et al., 2001). In order to estimate a coherence measure for a set of filtered EEG signals $F_{j,\omega,e}$ we first subtract their mean across the whole time segment:

$$F'_{j,\omega,e}(t) = F_{j,\omega,e}(t) - \sum_{t'=1}^{N_t} F_{j,\omega,e}(t'). \tag{12}$$

Then for each trial j we take the zero-lag coherence on a time window around time t which is given by

$$\mu_{j,\omega,e_1,e_2}(t) = \frac{|R_{j,\omega,e_1,e_2}(t)|}{|R_{j,\omega,e_1,e_1}(t)R_{j,\omega,e_2,e_2}(t)|^{1/2}} \tag{13}$$

where

$$R_{j,\omega,e_1,e_2}(t) = \frac{1}{2w+1}\sum_{t'=t-w}^{t+w} F'_{j,\omega,e_1}(t')(F'_{j,\omega,e_2}(t'))^*, \tag{14}$$

for each time t and electrode pair (e_1, e_2). A window size of 105 ms was also used for coherence measures.

2.9. Bayesian estimation of significant synchrony

Since we are interested in event-related activity, we must determine how significant are the changes of synchrony with respect to the pre-stimulus segment. To do this, we subtract the average synchrony in the pre-stimulus segment in order to obtain the relative synchrony X_{j,ω,e_1,e_2}:

$$X_{j,\omega,e_1,e_2}(t) = \mu_{j,\omega,e_1,e_2}(t) - \frac{1}{T_s}\sum_{t'=1}^{T_s}\mu_{j,\omega,e_1,e_2}(t'), \tag{15}$$

where T_s is the length of the pre-stimulus segment. Finally, we take the mean relative synchrony Y_{ω,e_1,e_2} across all trials:

$$Y_{\omega,e_1,e_2}(t) = \frac{1}{N_r}\sum_{j=1}^{N_r} X_{j,\omega,e_1,e_2}(t). \tag{16}$$

In order to estimate the significance of the Y-values, it is common to compute the p-value of each Y with respect to a null distribution and apply a threshold to them. In our case, the null distribution comes from the pre-stimulus segment (for each frequency and electrode pair), which by construction is centered at zero. Y-values which are "too positive" with respect to the null distribution correspond to significant synchrony increases, and similarly, "too negative" Y-values correspond to significant synchrony decreases.

To simplify interpretation and visualization, we would like to classify each Y-value in one of three classes: significantly higher (class $c = 1$), significantly lower (class $c = -1$), or equal ($c = 0$) to the pre-stimulus average. One possibility would be to simply apply a threshold to the p-values as mentioned above; however, we have chosen instead to use a more sophisticated classification method that permits one to impose additional constraints to control the granularity of the results. In particular, one would like that only those synchronous episodes with a duration greater than a minimum (physiologically motivated) value should be considered significant. According to studies related, for example, with the formation of short term memory (Jensen et al., 1996; Burle and Bonnet, 2000), this minimum value is in the order of one gamma oscillation, that is, around 20–50 ms.

It is worth noting that our final implementation of the classification method is relatively simple and efficient, as will be shown later.

A common technique for classification problems consists of Bayesian estimation with a prior Markov random field (MRF) model (Marroquin et al., 1987, 2001, 2004). With this method, one can model the class field $c_{\omega,e_1,e_2,t}$ as a random field with a prior Gibbs distribution of the form

$$P_{\mathrm{MRF}}(c) = \frac{1}{Z}\exp\left[-\lambda\sum_{C} V_C(c)\right], \tag{17}$$

where Z is a normalizing constant and V_C is a potential function that depends only on the values of the sites belonging to the clique C (a clique is either a single site, or any group of sites all of which are mutual neighbors, see Marroquin et al., 1987, 2001 for more details). For a classification problem, a popular model is the Ising model which enforces c to be piece-wise constant. If we consider a first-order neighborhood system, whose cliques are single sites and nearest neighbor pairs, the Ising potentials are given by:

$$V_{t,t'}(c) = \begin{cases} -1, & \text{if } c_{\omega,e_1,e_2,t} = c_{\omega,e_1,e_2,t'} \\ 1, & \text{if } c_{\omega,e_1,e_2,t} \neq c_{\omega,e_1,e_2,t'} \end{cases}, \tag{18}$$

where t and t' are adjacent sites in the time dimension. At this point, we are only interested in modeling persistence in time, and thus one can estimate the time-series $c_t = c_{\omega,e_1,e_2,t}$ in a decoupled manner for each frequency ω and electrode pair $\langle e_1, e_2\rangle$. However, it is also possible (although computationally expensive) to add constraints to model the consistency of c across different frequencies and/or across the spatial dimensions, in order, for example, to perform an automated segmentation of the TFT space.

Given prior probabilities $\alpha_k = P(c_t = k)$, the posterior distribution of c given Y can be calculated as

$$P(c|Y) = \frac{1}{Z'}\exp\left[\sum_t \log\, h_t(c_t) - \lambda\sum_{\langle t,t'\rangle} V_{t,t'}(c)\right], \tag{19}$$

where Z' is a normalization constant and $h_t(k) = P(Y_t \mid c_t = k)\alpha_k$.

The optimal estimator $\hat{c}$ can be found by maximizing the posterior marginal distribution $\pi_t(\hat{c}_t) = \sum_{c:c_t=\hat{c}_t} P(c \mid Y)$ for each t. This Maximizer of Posterior Marginals (MPM) estimator is usually approximated using stochastic Markov-chain methods such as Metropolis or the Gibbs sampler. These algorithms, however, are computationally expensive and require an unknown number of iterations, which makes them less than adequate for our multidimensional data set. A better solution consists on approximating the posterior marginal distributions with the *empirical marginals* $p_t(k)$ (Marroquin et al., 2001) which also form a MRF with the same neighborhood system as c and can be found by minimizing the energy function $U(p)$ given by:

$$U(p) = \sum_t |p_t - \hat{p}_t|^2 + \lambda'\sum_{\langle t,t'\rangle} |p_t - p_{t'}|^2, \tag{20}$$

with $\hat{p}_t(k) = h_t(k)/\sum_{k'} h_t(k')$.

Since each $p_t(k)$ is continuous, $U(p)$ can be minimized by solving the linear system obtained from equating the partial derivatives of U with respect to $p_t(k)$ to zero. Noting, however, that the optimal time-series $p(k)$ is a smoothed version of $\hat{p}(k)$, one can achieve a similar result by simply low-pass filtering each $\hat{p}(k)$ with a Gaussian kernel (for more details see Marroquin and Figueroa, 1997). The width of the Gaussian kernel will replace the model parameter λ' and will control the granularity of the results. In our case, we set this parameter so that blocks with constant c-values of length less than 25 ms occur less than 5% of the time (see Alba et al., 2006 for details).

Once we have p we can obtain the approximated MPM estimator as

$$c_t = \mathrm{argmax}_k\{p_t(k)\}. \tag{21}$$

2.10. Estimation of prior distributions and likelihoods

In order to calculate $h_t(k)$ (and thus $p_t(k)$) we need the prior probabilities α_k and likelihoods $P(Y_t \mid c = k)$. These can be estimated from the data if we consider that the complete distribution $P_Y(Y_t)$ can be expressed as:

$$P_Y(Y_t) = \sum_{k=-1}^{1} \alpha_k P(Y_t \mid c = k), \tag{22}$$

and also consider the following assumptions:

- $P(Y_t \mid c = 0)$ may be estimated empirically from the pre-stimulus data.
- $P(Y_t \mid c = 1) = 0$ for $Y \leq 0$.
- $P(Y_t \mid c = -1) = 0$ for $Y \geq 0$.

With these assumptions, we can obtain $P(c = 0)$ from Eq. (22) as follows:

$$\alpha_0 = \frac{P_Y(0)}{P(0 \mid c = 0)} \tag{23}$$

and also

$$h_t(0) = \alpha_0 P(Y_t \mid c = 0) \tag{24}$$

$$h_t(1) = \begin{cases} P_Y(Y_t) - h_t(0), & Y_t > 0 \\ 0, & Y_t \leq 0 \end{cases} \tag{25}$$

$$h_t(-1) = \begin{cases} P_Y(Y_t) - h_t(0), & Y_t < 0 \\ 0, & Y_t \geq 0 \end{cases} \tag{26}$$

$P_Y(Y_t)$ and $P(Y_t \mid c = 0)$ can be estimated from the data Y using non-parametric kernel estimation: the distribution p_Y is estimated from the sample $\{Y_t\}$ as the sum of superimposed kernel functions k_h centered at each Y_t. In other words,

$$p_Y(y) = \frac{1}{Z} \sum_{i=1}^{N_t} k_h(y - Y_t), \tag{27}$$

where Z is a normalization constant chosen so that p_Y integrates to 1. The parameter h specifies the width of the kernel and determines the smoothness of p_Y. Adequate choice of h depends on the sample data; however, for automated applications, a rule of thumb for a Gaussian kernel (which we use) is provided by (Silverman, 1986):

$$h_{\text{opt}} = 1.06\sigma n^{-1/5},$$

where σ is the standard deviation of X (estimated from the sample). Note that $P_Y(Y_t)$ is estimated using the full time segment, whereas $P(Y_t \mid c = 0)$ is estimated by considering only the pre-stimulus segment.

The actual classification procedure for significative synchrony changes is performed (for each frequency ω and electrode pair $\langle e_1, e_2 \rangle$) as follows:

1. Estimate the pre-stimulus distribution $P_0(Y)$ and the full distribution $P_Y(Y)$ using kernel density estimation with bandwidth given by Silverman's rule of thumb.
2. Estimate $\alpha_0 = P(c = 0) = P_0(0)/P_Y(0)$.
3. For each t, calculate $h_t(k)$ for $k = -1, 0, 1$ as given by Eqs. (24)–(26).
4. Normalize h_t to obtain $\hat{p}_t$ for all t.
5. Obtain $p(k)$ by convolving $\hat{p}(k)$ with a Gaussian kernel g. The width σ of the filter controls the granularity of the c field.
6. Approximate the MPM estimator by $c_t = \text{argmax}_k\, p_t(k)$ for all t.

This procedure yields results that are roughly similar to those obtained by directly thresholding the p-values (with a threshold between 0.01 and 0.1); however, the value of the threshold (critical p-value) that yields the desired granularity (e.g. synchronous episodes which last at least 25 ms) varies for different data sets, and has to be set in an empirical way for each particular case.

It should also be noted that the parameter σ, which controls the granularity in the Bayesian method is not critical: one obtains very similar classifications for a wide range of values of this parameter, whereas classification based on z-scores or p-values is in general more sensitive to the precise value of the threshold.

2.11. Visualization

For a fixed time t and frequency ω it is possible to show the distribution of the synchrony pattern (SP) given by the class values $c_{\omega,e_1,e_2,t}$ in a multitoposcopic display, in which for each electrode e_1 one displays a head diagram (also called "toposcope") – within a bigger head – that shows the distribution of c across all sites e_2 (an example of this display can be seen in Fig. 2a).

A problem arises when one deals with high electrode density recordings since only so many toposcopes can be displayed within the bigger head. One can use interpolation techniques to display high-density data in a single toposcope (in particular, we use a Voronoi partition Aurenhammer, 1991, obtained by assigning each pixel in the toposcope the class corresponding to the nearest electrode), but the number of toposcopes may have to be reduced. One possibility consists in grouping the electrodes in N_g cortical areas $\{G_1, \ldots, G_{N_g}\}$, using again a Voronoi partition whose centers are, for example, the sites Fp1, Fp2, F3, F4, C3, C4, P3, P4, O1, O2, F7, F8, T3, T4, T5, T6, Fz, Cz, and Pz of the 10/20 system. One can then plot a toposcope for each group G_k computing, for each high-resolution electrode, the "most representative" synchrony class between this electrode and the electrodes in G_k. This most representative class may be computed in several ways; for example, the average class $\bar{c}$ of electrode e to group G_k which is computed as:

$$\bar{c}_{\omega,k,e,t} = \frac{1}{|G_k|} \sum_{e' \in G_k} c_{\omega,e',e,t} \tag{28}$$

or the class mode $\hat{c}$, which is computed as:

$$\hat{c}_{\omega,k,e,t} = \text{argmax}_{q \in \{-1,0,1\}} \left\{ \sum_{e' \in G_k} \delta(c_{\omega,e,e',t} - q) \right\}, \tag{29}$$

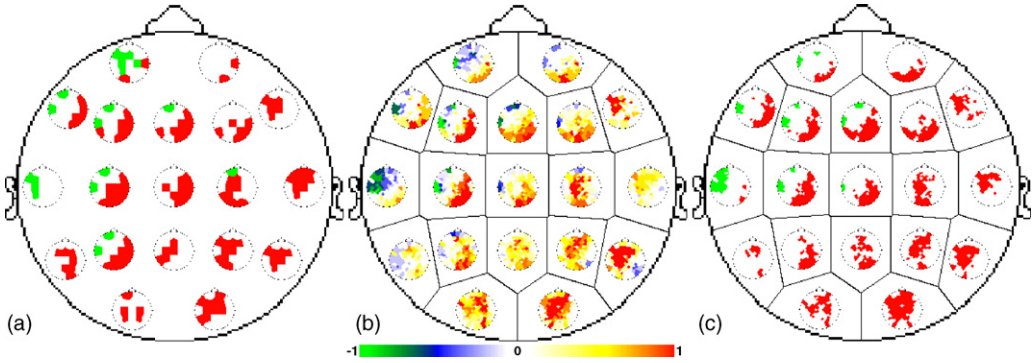

Fig. 2. Multitoposcopic displays for a 120-channel dataset using the MPD measure: (a) uses only channels Fp1, Fp2, F3, F4, C3, C4, P3, P4, O1, O2, F7, F8, T3, T4, T5, T6, Fz, Cz, and Pz from the 10/20 system: red regions represent electrode pairs that show a significant increase in synchrony ($c = 1$), while green regions correspond to significant synchrony decreases ($c = -1$). Graphs (b and c) use the 120 channels grouped in 19 cortical areas corresponding to the Voronoi partition whose centers are the electrodes used in (a). For each area, one can plot a toposcope representing a statistic of the synchrony classes between each of the 120 electrodes and the electrodes within the area: (b) uses the average class $\bar{c}$ (which may be between -1 and 1), whereas (c) uses the class mode $\hat{c}$ (see text for details). The three multitoposcopes represent the SP obtained at $t = 515$ ms and $f = 11$ Hz during a Go/NoGo experiment; the rest of the examples presented in this paper correspond to the Figures experiment described in the text.

where δ is the Kronecker delta function. An example of multitoposcopes corresponding to $\bar{c}$ and $\hat{c}$ are shown in Fig. 2b and c. More sophisticated methods could involve electrode clustering or TFT regularization; however, they are beyond the scope of this paper.

Multitoposcopic displays are useful to show a detailed connectivity pattern for a fixed time and frequency; however, it is important to visualize larger regions of the time–frequency plane in order to localize zones of interest where the synchrony pattern remains almost constant and might be related to specific cognitive processes. For this purpose, we can use a time–frequency-topography (TFT, Marroquin et al., 2004) display to present the data by reducing only one spatial dimension. We do this by counting, for each site e, the number of sites whose synchrony with e has significantly increased (or decreased). In other words, we can build a *synchrony increase histogram* (SIH) given by

$$H^{+}_{\omega,e}(t) = \sum_{e'=1}^{N_e} I(c_{\omega,e,e',t} = 1), \tag{30}$$

where $I(P) = 1$ only if P is true. $H^{+}_{\omega,e}(t)$ is the number of significantly stronger couplings (with respect to the pre-stimulus segment) for site e at time t and frequency ω. Similarly, we can define a *synchrony decrease histogram* (SDH) as

$$H^{-}_{\omega,e}(t) = \sum_{e'=1}^{N_e} I(c_{\omega,e,e',t} = -1), \tag{31}$$

These histograms can be presented in a TFT display as shown in Figs. 3 and 4.

Another option is to divide the TF plane in regions, and display a representative SP for each region (for example, the average SP, or the SP that corresponds to the center of the region). An example of this type of display is presented in Fig. 5, where the TF plane has been partitioned by frequency bands and at regular 300 ms intervals.

2.12. Comparison between synchrony measures

Fig. 6 show the SIH's for the MPD, CPPD, PLS, STPLS, and coherence measures. It is clear that CPPD and PLS give very similar results to the MPD measure. On the other hand, STPLS and coherence yield similar results themselves but different from MPD. The estimated correlation between each pair of measures (Fig. 7, left) confirms what we see. It is worth noting that similar correlation results were also obtained with five different experiments besides the Figures experiment presented here (see Alba et al., 2006 for details).

Seemingly, we have two groups of synchrony measures; thus it is important to understand what kind of similarities between signals are being quantified by each group, and how measures from the same group are related to each other. One thing to note is that STPLS and coherence are defined across a time window, while the other measures are "instantaneous". Because of this, STPLS and coherence may be less sensitive to trial-to-trial latency jitter, which characterizes induced responses (i.e., those that are not phase-locked to the stimulus). Typically, induced activity is revealed by performing a time–frequency decomposition of each trial, and averaging a positive definite function of the filters' output (e.g., the power) across all trials, whereas evoked activity is obtained by first averaging the raw signals across trials, and then applying a positive definite function (power analysis) to the average signals (David et al., 2006). The difference is that in the former case (induced responses) there will be no cancellations during averaging, whereas in the latter (evoked) case, there may be cancellations due to differences in sign across trials. It is clear then, that the methodology presented in the previous sections is basically an induced response analysis, where the positive definite function is the synchrony measure (we may call it "induced synchrony"), instead of the power; this function is averaged across trials and then the baseline is subtracted. This suggests that our procedure, with any of the synchrony measures presented here, should be at least as sensitive to induced responses as the typical average-power analysis. Of course, because of additional averaging across time, STPLS

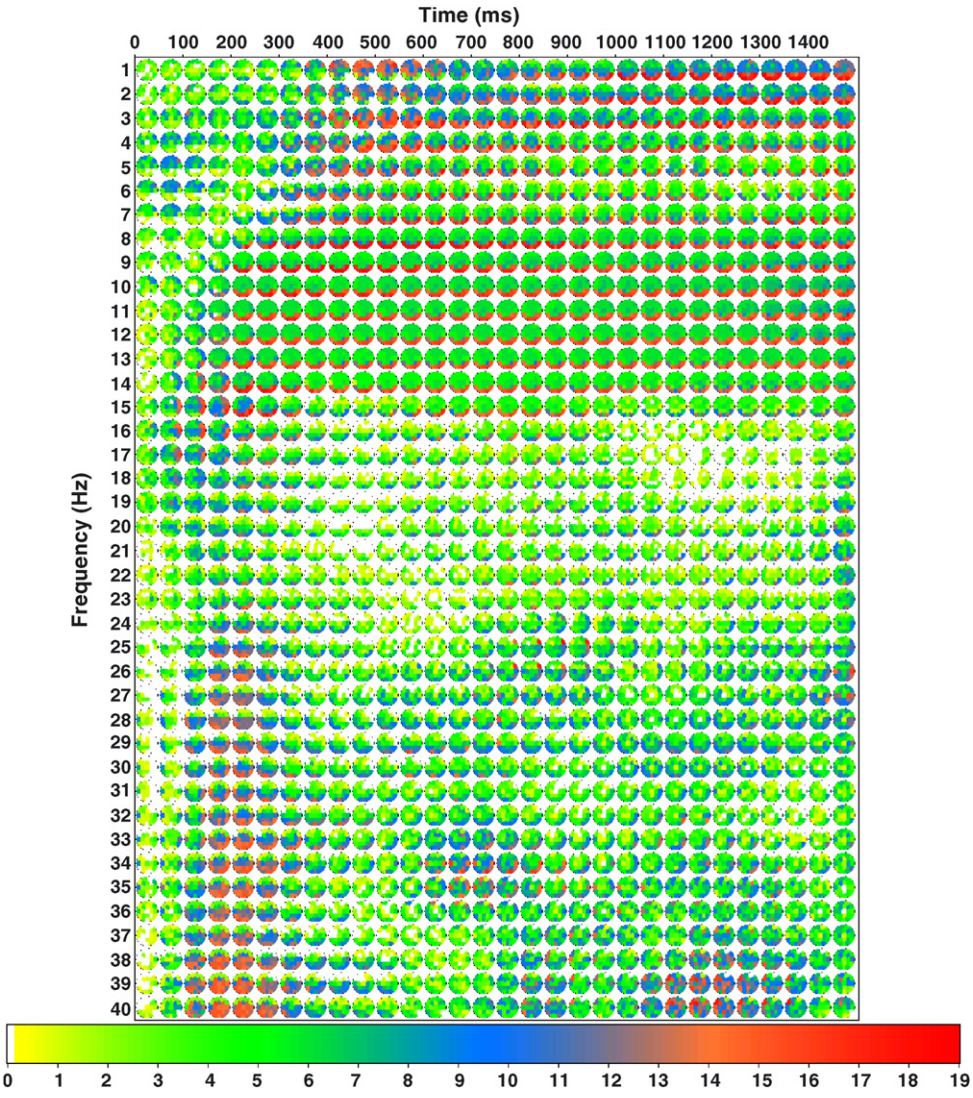

Fig. 3. Synchrony increase histogram for the Figures experiment. The color scale represents, for each recording site e, the number of sites that show a significant increment in synchrony (class $c = 1$) with e. There are 20 recording sites in the Figures experiment, thus each site may increase its synchrony with at most 19 other sites.

and coherence may be more robust to larger amounts of latency jitter.

A problem with the coherence and STPLS measures is that they may decrease their value (i.e., they may signal a spurious decoupling) if the local phase dispersion of either one of the two electrodes under consideration increases and vice versa. In particular, if the phase of one electrode in the STPLS measure (Eq. (11)) remains relatively constant across the time window, then this measure will be related to the dispersion of the other phase. To see how much this variance influences the STPLS, we estimated a local phase constancy (LPC) measure for each electrode, which equals one minus the local phase dispersion across a time window:

$$\mathrm{LPC}_{j,\omega,e}(t) = \frac{1}{2w+1}\left|\sum_{t'=t-w}^{t+w} \exp[\mathrm{i}\phi_{j,\omega,e}(t')]\right|. \quad (32)$$

Fig. 6 (bottom-right graph) shows the TFT map of significant LPC changes: red and green spots indicate significant increases and decreases, respectively, in the phase constancy across time. Note that red regions in the LPC map correspond to increases in STPLS and coherence. The green region in the alpha band in the LPC map also corresponds to a decrease in synchrony observed in the STPLS and coherence SDH's (not shown).

We estimated the correlation between the LPC changes and the average synchrony changes at each electrode for all the measures (Fig. 7, right). Effectively, both STPLS and coherence show high correlation with LPC, as well as a slightly higher correlation with amplitude changes (Marroquin et al., 2004) (which makes sense for coherence, since it uses both the magnitude and phase of the signals). This suggests that measures such as MPD and CPPD may be more specific for the detection of in-phase synchronous episodes, since they are less influenced by the temporal phase dispersion that may occur on one of the electrodes of the pair under study.

By looking at Eq. (10) one can see that PLS actually measures the consistency of the phase difference across all trials. We have also shown that the MPD and PLS measures are highly corre-

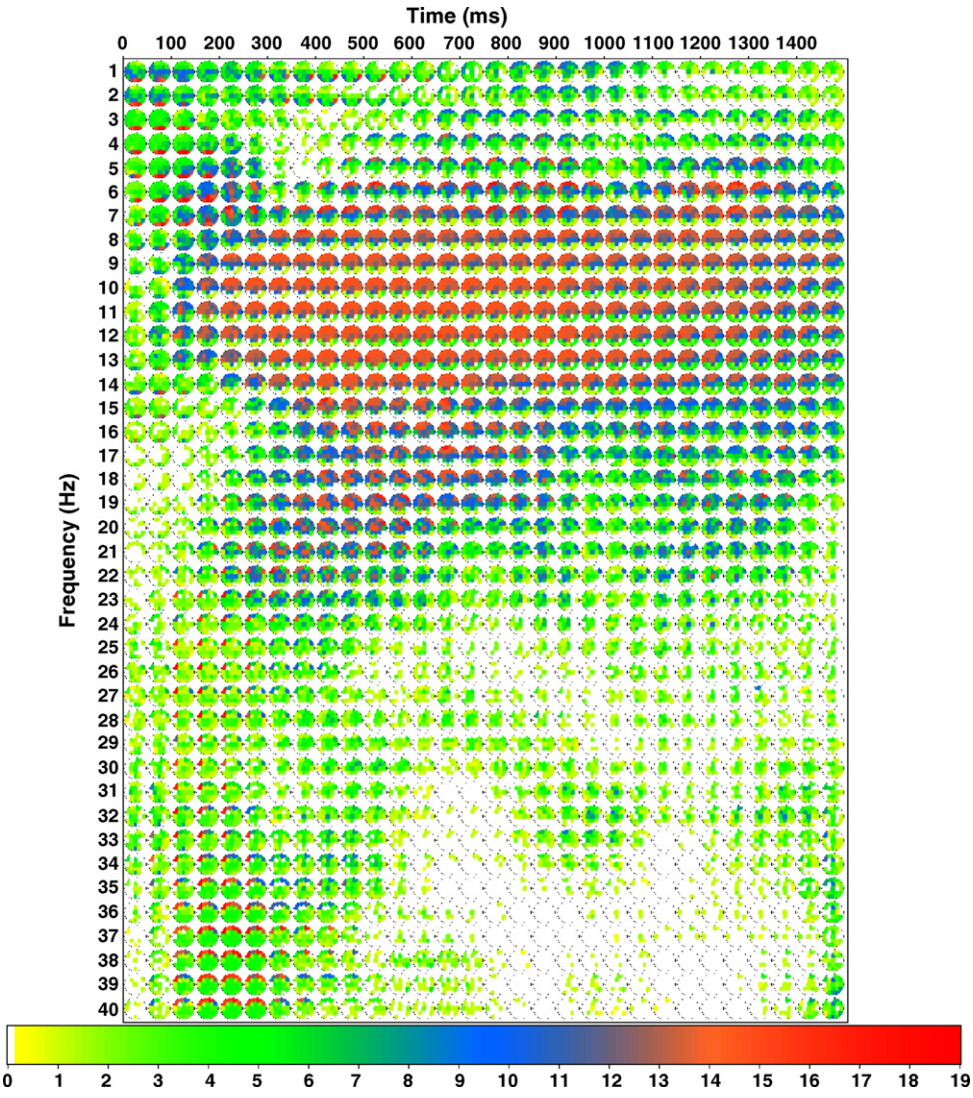

Fig. 4. Synchrony decrease histogram for the Figures experiment. The color scale represents, for each recording site e, the number of sites that show a significant decrease in synchrony (class $c = -1$) with e.

lated. This suggests that the processes that result in high synchronization (as measured by MPD) are fairly consistent across trials and subjects, and thus may be related to the task.

Furthermore, the CPPD measure is also highly correlated to the MPD, suggesting that synchronization effectively happens with near-zero phase difference. This is in accordance with the neural mass model proposed by David and Friston (2003) and other works (Friston et al., 1997; Rodriguez et al., 1999) which have also found zero-centered phase difference distributions during synchronous episodes between two electrodes.

Another important issue which directly affects the detection of EEG synchrony is the volume conduction (Nunez, 1995): the conductive properties of the cortex, skull, and scalp produce a smearing of the potentials across the surface, which may result in spurious correlations between EEG signals, especially between neighboring sites.

Nunez (1995, 2000), Nunez et al. (1997) have developed an extensive work on the effect of volume conduction in EEG coherence. Using simulated data from a three concentric spheres model, they estimated correlation coefficients for pairs of uncorrelated cortical sources using different EEG references (Cz, neck, linked ears, and average reference), cortical imaging, and Surface Laplacians (SL, (Perrin et al., 1989, 1990; Law et al., 1993). In all cases, except SL, spurious high correlations were observed for short inter-electrode distances (4–8 cm) (Nunez et al., 1997). However, since the potentials are relatively smooth across the surface (partly because of volume conductor effects), the SL, which is the second spatial derivative of the potentials, may have a relatively small magnitude, and thus may be more vulnerable to noise than the scalp potentials (Junghöfer et al., 1999). It is also worth stressing that accurate SL estimation requires high spatial sampling density (64–128 channels) (Law et al., 1993; Nunez, 1995; Junghöfer et al., 1999).

Since the SL acts as a bandpass filter on the raw potentials, true coherence with low spatial frequency (i.e., relatively smooth across the surface) may be underestimated. Because of this, Nunez suggests to use the SL to complement, rather than replace, the raw EEG potentials: correlations may be observed at different spatial scales (Nunez et al., 1997; Nunez, 2000) (just as correlations between customs of people from two different

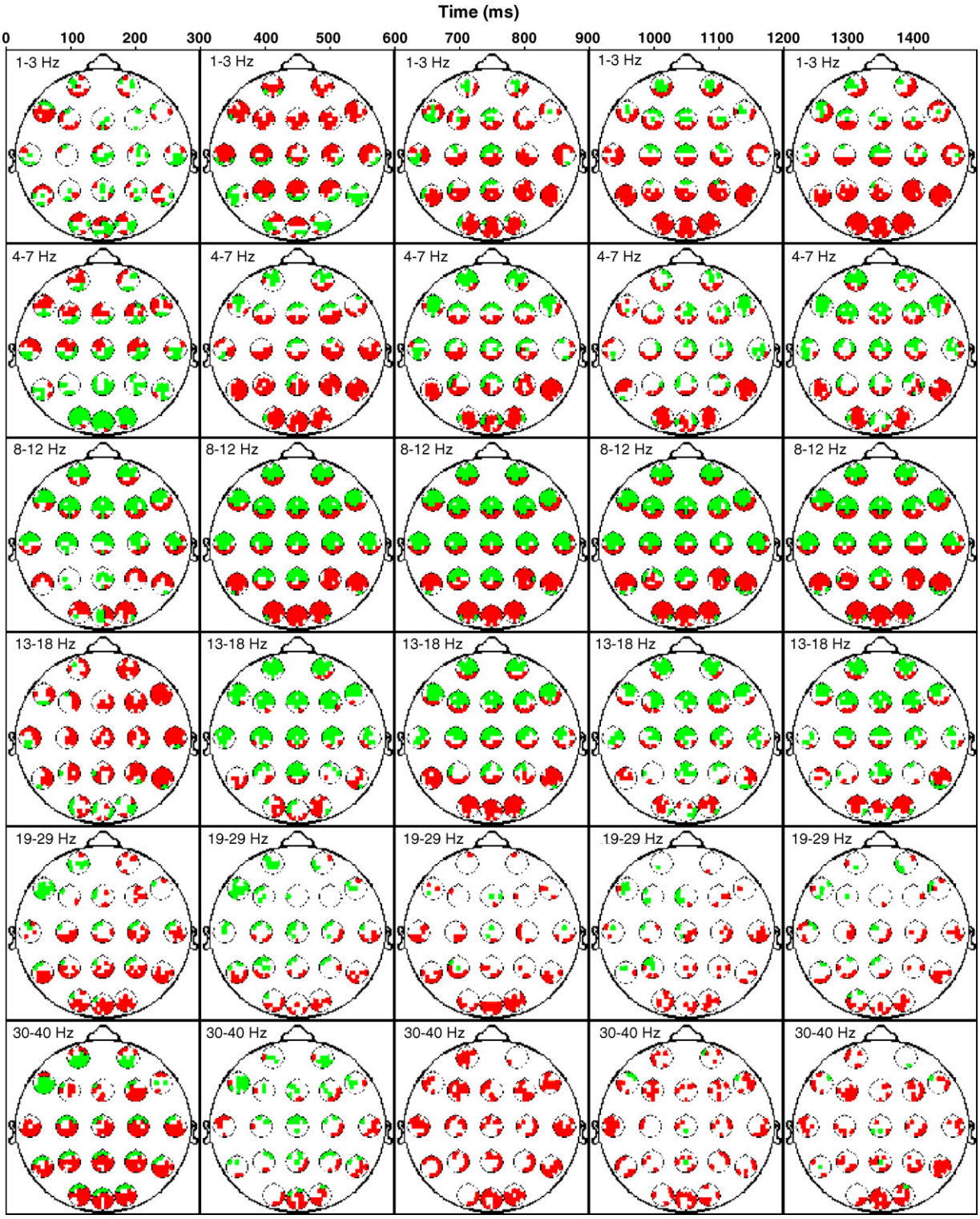

Fig. 5. Subdivided synchrony map for the Figures experiment. The TF plane is partitioned by frequency bands and at each 300 ms. The displayed SP in each region corresponds to the center point of the region.

cities may differ from correlations between two families, one from each city). Therefore, raw potential, Surface Laplacian, and cortical image coherency may, in general, represent correlations at different spatial scales of cortical dynamics.

Although these studies by Nunez focus only on coherence, it is reasonable to think that the volume conductor also has a significative influence on other synchrony measures. One may think that a synchronization measure that favors phase differences equal to zero (e.g. MPD or CPPD) might be more sensitive to volume conduction. However, this is not necessarily true, since if several sources influence two different sites via volume conduction, their net influence on the resulting electrode signals

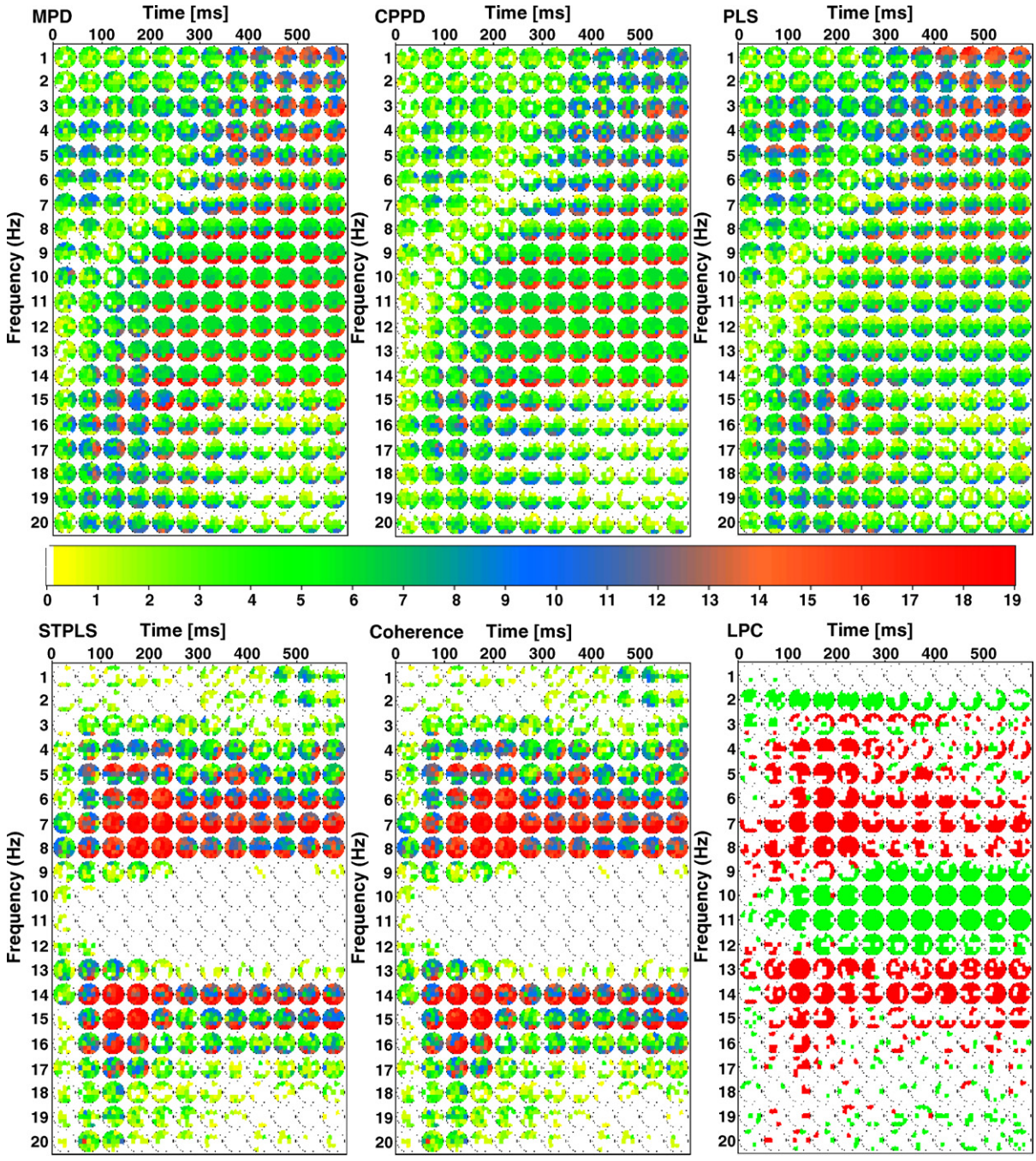

Fig. 6. Synchrony increase histograms for the Figures experiment using the five synchrony measures: MPD, CPPD, PLS, STPLS, and coherence. The bottom-right graph corresponds to the TFT map of significant changes in the LPC measure (red represents significant increases, whereas green corresponds to significant decreases), see text for details.

	MPD	CPPD	PLS	STPLS	Coherence
MPD	1.000	0.835	0.853	0.477	0.508
CPPD	0.835	1.000	0.755	0.500	0.525
PLS	0.853	0.755	1.000	0.503	0.536
STPLS	0.477	0.500	0.503	1.000	0.872
Coherence	0.508	0.525	0.536	0.872	1.000

	LPC	AMP
MPD	0.102	-0.019
CPPD	0.067	-0.114
PLS	0.131	0.067
STPLS	0.698	0.266
Coherence	0.673	0.273

Fig. 7. Correlation between pairs of synchronization measures (left), and between synchronization measures and local phase constancy or amplitude (power) changes (right). There are clearly two groups of measures: those similar to the MPD, and those similar to the STPLS. The latter group is characterized by a high correlation with LPC and a slightly higher correlation with power changes.

will correspond to different linear combinations of these source signals (with coefficients given by the corresponding attenuations), thus producing different phases (Lachaux et al., 1999; see also the discussion below on apparent phase). Furthermore, the MPD and CPPD measures are highly correlated to Lachaux's PLS measure, which measures synchrony with a constant phase lag (not necessarily zero), suggesting that at least these three measures are similarly affected by volume conduction. Lachaux also suggests that one may be able to identify conduction synchrony by looking at the neighboring sites of the two electrodes under analysis: if conduction synchrony is observed between two electrodes, then one should also observe high synchrony between their neighbors. To test this, we have estimated a cross-neighbor synchrony measure Z^+ given by:

$$Z^+_{\omega,e_1,e_2,t} = \frac{\sum_{k\in N_1, j\in N_2} I(c_{\omega,e_k,e_j,t} = 1)}{|N_1\|N_2|} \cdot I(c_{\omega,e_1,e_2,t} = 1) \tag{33}$$

where $I(P)$ equals 1 if P is true and zero otherwise, and N_i is the set of neighboring sites for e_i (we have chosen a neighborhood radius such that each e_i has at least one neighbor). In other words, $Z^+_{\omega,e_1,e_2,t}$ represents the proportion of neighbor-pairs which show a significant increase of synchrony when e_1 and e_2 increase their synchrony. The c-values used to estimate Z^+ were obtained from thresholded p-values ($\alpha = 0.01$) to avoid any bias that may be introduced by the regularization constraints of the Bayesian method. One can then estimate the average Z^+ across all electrode pairs which show a significant increase of synchrony. Interestingly, STPLS and coherence produced the highest average values (around 0.16), while CPPD and PLS corresponded to the lowest (between 0.06 and 0.1). According to these tests, one therefore cannot conclude that a MPD or CPPD are more sensitive to conduction synchrony than the other measures.

All these findings lead us to believe that MPD and CPPD are suitable measures for long-range synchronization.

3. Discussion

A full analysis of the Figures experiment using the MPD measure is presented here as an example of the methodology. The full segmented MPD map is presented in Fig. 5 along with the corresponding SIH and SDH maps (Figs. 3 and 4, respectively). The TFT map of significant changes in amplitude is also shown in Fig. 8.

Recall that we are measuring the changes in synchrony during a particular state in relation to a previous condition that we may consider as neutral. It is possible to observe changes in phase-lock at all frequencies. Synchrony increases in the delta band in the anterior regions between 450 and 600 ms. After this time, the synchrony increased mainly in the posterior regions (Fig. 3). In the first 150 ms in the delta and theta bands there was a decrease in synchrony in occipital regions (Fig. 4). This may be due to the activation of the visual areas produced by the stimuli. In the theta range (4–7 Hz), the most generalized change in synchronization in the EEG after 300 ms is the phase-lock increase between posterior and anterior regions, which can be observed in the partitioned map (Fig. 5). This pattern may be related to activation of working memory (WM), which is the process of actively maintaining a representation of information for a brief period of time so that it is available for use. Attention, decoding, perception and maintenance in memory are processes that involve the activation of WM. Visual working memory involves the concerted activity of a distributed neural system, including posterior areas in visual cortex and anterior areas in prefrontal cortex (Ungerleider et al., 1998).

The increase in theta power in frontal regions has been related to activation of WM (Gevins et al., 1997; Rhom et al., 2001). Anterior regions are also involved in encoding (Klimesch et al., 2004) and maintaining the information in memory (Barde and Thompson-Schill, 2002). An increase in coherence in the theta range was found by Sarnthein et al. (1998) between prefrontal and posterior electrodes during retention of a string of characters.

In the alpha range, simultaneously with the increase in synchrony in the occipital regions, there was a decrease in synchrony between all regions except the occipital leads and the frontal regions on which synchrony increases. This increase may be indicating the projection loops between attentional control system in prefrontal cortex and activated meaning representations in semantic memory in posterior regions. The decrease in synchrony in the alpha band between 100 and 1500 ms coincides with the phenomena described in the 1930s by Adrian and Mathews of amplitude decrease or "desynchronization" and it has been related to attention (Gevins et al., 1997; Rhom et al., 2001; Klimesch, 1999).

Other change that was observed is the increase of synchrony in occipital regions in the beta band. In humans, in intracranial recordings that limited regions of extrastriate visual areas, separated by several centimeters, EEG activity in the beta range (15–25 Hz) became synchronized in an oscillatory mode during the rehearsal of an object in visual short-term memory. According to Tallon-Baudry et al. (2001) these findings confirm experimentally the hypothesis of a functional role of synchronized oscillatory activity in the coordination of distributed neural activity in humans, and support Hebb's (1949)popular concept of short-term memory maintenance by reentrant activity within the activated network.

In the gamma band an increase of synchrony in the interval 200–300 ms was observed. This increase in synchrony in the gamma band has been related to visual search and perception (Tallon-Baudry et al., 1997). The increase in synchronization during the interval of 600–800 ms in the gamma band might be related to preparation of the motor response.

From the analysis of these and other experimental data (see Alba et al., 2006 for details), one observes certain phenomena that may appear counter-intuitive; for example:

1. Synchronous episodes occur with near-zero phase lag, regardless of the distance between leads.
2. It is possible to have two (or more) electrodes increasing their synchrony with a third one (which acts as a nodal point), and at the same time, observe a decrease of synchronization between the non-nodal leads (see, for example, the SP associ-

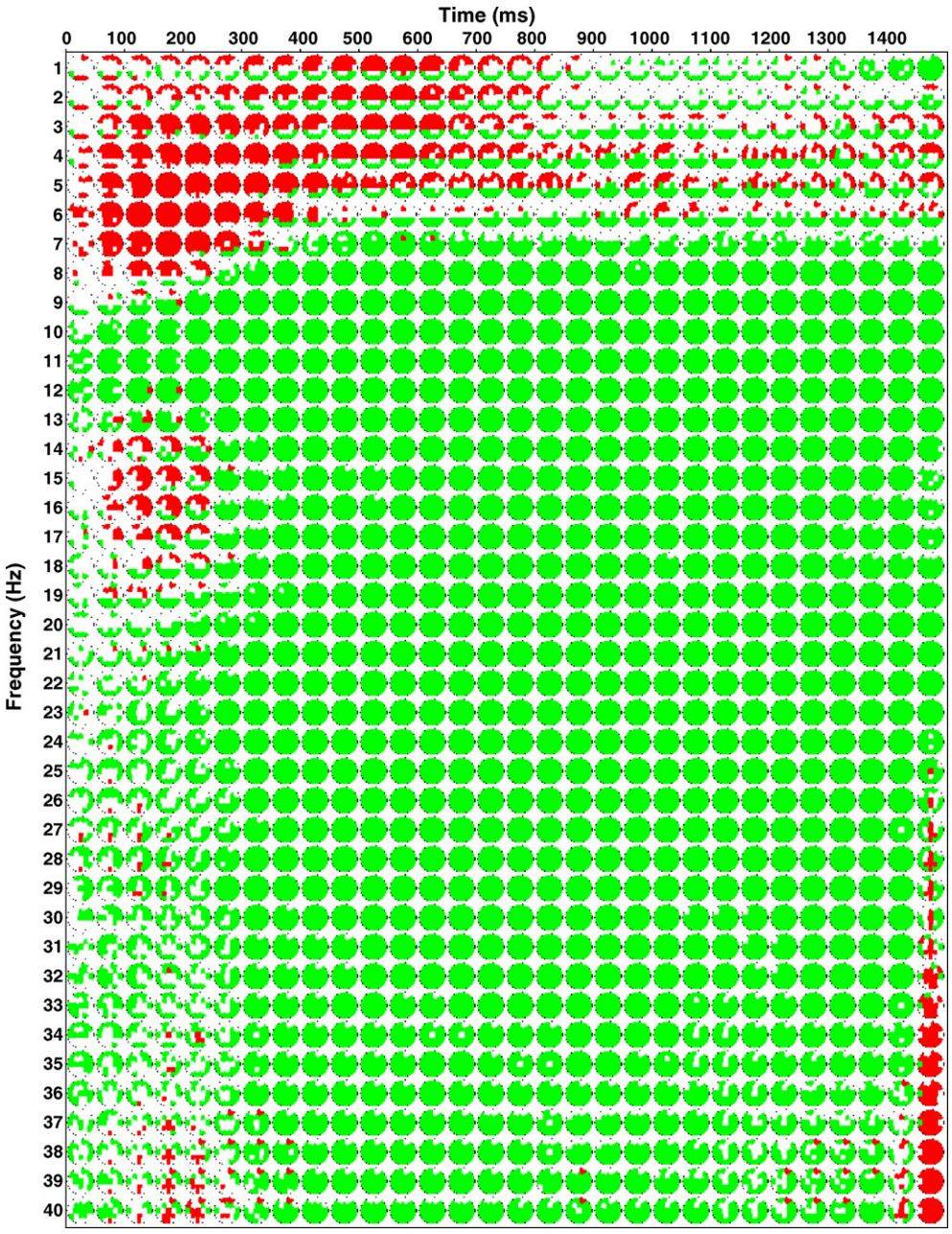

Fig. 8. Map of significant amplitude changes for the Figures experiment: sites whose amplitude is significantly higher than the pre-stimulus average are shown in red (dark gray in the printed version) while those with significantly lower amplitude are shown in green (light gray in the printed version).

ated to the alpha band in Fig. 5, where occipital leads increase their synchrony with most of the other leads, while fronto-parietal leads show a decrease of synchrony among them). This phenomenon can also been observed in other studies, such as Rodriguez et al. (1999) and David et al. (2003).

3. When a single electrode *e* increases its synchrony with many sites, there is a high probability of a power decrease at *e*.

These phenomena may be explained by the following considerations: a scalp electrode provides estimates of synaptic action averaged over tissue masses containing between 10^7 and 10^9 neurons (Nunez, 1995). Moreover, there is evidence (obtained, for example, using retrogradely transported fluorescent dyes Morecraft et al., 1993, and single-cell recordings Quintana and Fuster, 1999) of extensively intermingled populations of neurons connected with different areas (e.g., frontal eye fields and posterior parietal cortex). Moreover, when performing a computational task, neurons may quickly associate into a functional group while disassociating from concurrently activated groups (Haalman and Vaadia, 1998).

All these facts suggest that the signal recorded by a scalp electrode may in fact result from a sum of macroscopic oscillations produced by functionally different neural populations (which may be histologically intermingled). Since each one of these sub-populations must be synchronized so that a macroscopic oscillation develops, a reasonable model for a complex

band-pass EEG signal (i.e., the output of a narrow band-pass quadrature filter tuned at frequency ω) is:

$$S(t,\omega) = \sum_k \alpha_k e^{i(\omega t+\phi_k)}, \tag{34}$$

where the positive coefficients α_k depend on the amplitude and relative proportion of subpopulation k and ϕ_k is the corresponding phase.

The apparent amplitude $A(t,\omega)$ and phase angle $\phi(t,\omega)$ (obtained by subtracting ωt from the argument of the complex signal S) will be given by the resultant of the sum (on the complex plane) of the vectors $\alpha_k e^{i\phi_k}$:

$$A(t,\omega)\exp[i\phi(t,\omega)] = \sum_k \alpha_k(t)\exp[i\phi_k]. \tag{35}$$

This explains why the apparent phase difference between two synchronized distant regions is zero, in spite of the fact that there may be a significant transmission delay: with two sub-populations one can model a unidirectional coupling between two distant cortical areas, in the sense that a sub-population in one area drives a sub-population in the other area with a certain phase lag δ. For a bidirectional coupling we just add a reciprocal connection, with the same phase lag. Fig. 9 shows a schematic of two populations in bidirectional coupling. It can be shown that if all sub-populations have approximately the same size (i.e. $\alpha_k = 0.5$, $k = 1, 2$), then the apparent amplitude and phase for each electrode would be given by

$$A_1^* \exp[i\phi_1^*] = 2\cos\left(\frac{\phi^1-\phi^2}{2}\right)\exp\left[i\frac{\phi^1+\phi^2}{2}\right], \tag{36}$$

$$A_2^* \exp[i\phi_2^*] = 2\cos\left(\frac{\phi^1-\phi^2-2\delta}{2}\right)\exp\left[i\frac{\phi^1+\phi^2}{2}\right]. \tag{37}$$

So that $\phi_1^* - \phi_2^* \approx 0$, except in the case where

$$\frac{\phi^1-\phi^2+3\pi}{2} < \delta < \frac{\phi^1-\phi^2+\pi}{2},$$

in which case $\phi_1^* - \phi_2^* \approx \pi$, which is in accordance with (David and Friston, 2003).

This model for the apparent phase also explains the fact, which we have observed in all the experiments we have analyzed, that when a given site is synchronized with several other sites, in most cases there is also an amplitude decrease with respect to the baseline. These sites act as characteristic nodes of a particular network, hence we call them *nodal points*. To study this in detail, we define a site e as k-nodal at time t and frequency ω if it shows significant increase in synchronization with at least k different sites. Let N_k be the number of k-nodal points in the TFT space and A_k^- the number of k-nodal points that also show a power decrease; then the conditional probability of significant power decrease given that a site is k-nodal can be estimated by $P_k^- = A_k^-/N_k$. One may similarly estimate the conditional probability of power increment P_k^+. These probabilities are shown in Fig. 10 for the Figures experiment, where it is clear that P_k^- increases with the number of couplings k. The same behavior can be observed with three other experiments, all of which are presented in (Alba et al., 2006).

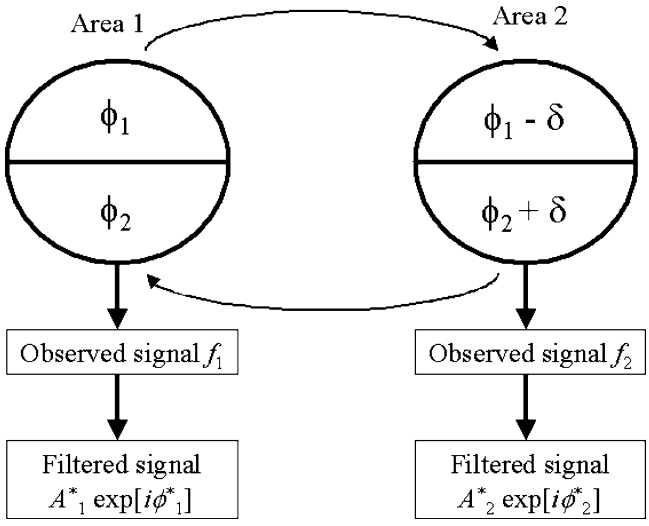

Fig. 9. Bidirectional coupling between two areas with two sub-populations each. If the sub-populations are approximately the same size, the apparent phase difference $\phi_1^* - \phi_2^*$ will be approximately 0 or π.

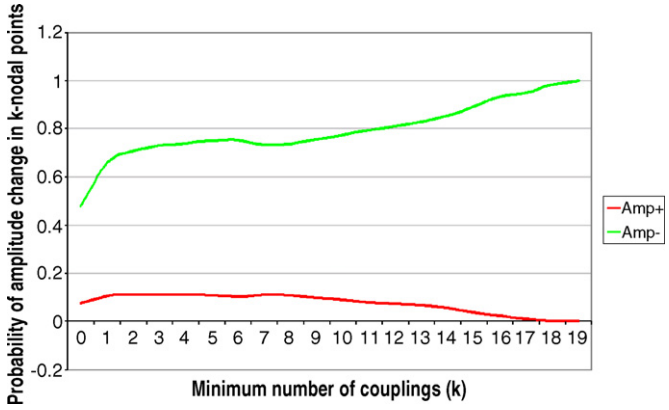

Fig. 10. Conditional probabilities of amplitude increment (red/dark gray) and decrease (green/light gray) in k-nodal points for the Figures experiment.

This behavior may be also be explained from Eq. (35): suppose the population covered by the nodal electrode is divided into various sub-populations, each one of which increases its synchrony (with respect to the baseline) with a different site. The relative dispersion of the non-nodal phases may not be different from that of the baseline, so that these sites may not exhibit any significant synchrony change among themselves; the apparent phase of the nodal point, however, will show increased synchrony with all these sites, and due to the non-nodal phase dispersion, the nodal point will show a significant apparent amplitude decrease as well. A more detailed analysis of this situation, including some simulations, is presented in (Alba et al., 2006).

4. Conclusion

Brain electroencephalographic activity changes as a function of state. During the performance of different tasks, several neuronal assemblies become active simultaneously. These neuronal networks are not necessarily contiguous and may occupy different cortical areas producing complex spatiotemporal patterns

of synchronization or desynchronization in relation to a previous state. Zero phase measurements between leads indicate that the EEG recorded in such leads became highly synchronized and may be integrating a network related to a particular psychophysiological process. Thus, phase relationships between regions may give important information about the dynamics of different cell assemblies.

The detection of these phase relationships must be performed with care. First, the time–frequency decomposition method should not introduce artifacts in the phase estimations. In this sense, sinusoidal quadrature filters have proven to be reliable. Second, there are two important aspects of synchrony estimation: the significance of the phase-lock measure, and its consistency across time. We believe that separating these two aspects provides better results, and we do this by means of an instantaneous phase-lock measure, and the inclusion of granularity constraints in the estimation of significance. On the other hand, phase-lock measures that are estimated across a time window may be contaminated by the effect of local phase dispersion. Volume conduction seems to have a similar effect on all the measures presented here; therefore, a more accurate assessment of synchrony may be obtained by complementing the analysis of raw potentials with Surface Laplacian estimates from high-density recordings, as suggested by Nunez (1995, 2000), Nunez et al. (1997). Unfortunately, most of our test datasets contain only 19 or 20 channels, which are not enough to compute an accurate SL. However, the methodological contributions presented in this paper remain valid for synchrony estimation if SL, current sources, or MEG signals are used instead of the raw scalp potentials. Finally, TFT visualization techniques have proven to be very useful for the analysis of cognitive tasks as they allow for a quick and interactive exploration of the TF plane while still providing spatial detail. The new insights in the Figures experiment and the nodal sites are examples of the usefulness of these tools.

Acknowledgements

We would like to thank Dr. Thalia Fernandez for data acquisition for the Figures experiment. J.L. Marroquin was supported by Conacyt grant no. 46270. A. Alba was supported by PROMEP, Mexico.

References

Alba A, Marroquin JL, Peña J, Harmony T. Analysis and visualization of EEG event-induced dynamic synchronization patterns in cognitive tasks. Technical communication no. I-06-05/08-03-2006 (CC/CIMAT). http://www.cimat.mx/reportes/enlinea/I-06-05.zip(zipped PDF), 2006.

Aurenhammer F. Voronoi diagrams—a survey of a fundamental geometric data structure. ACM Comput Surv 1991;23(3):345–405.

Barde LH, Thompson-Schill SL. Models of functional organization of the lateral prefrontal cortex in verbal working memory: evidence in favor of the process model. J Cogn Neurosci 2002;14:1054–63.

Bastiaansen M, Hagoort P. Event-induced theta responses as a window of the dynamics of memory. Cortex 2003;39:967–92.

Bressler SL, Coppola R, Nakamura R. Episodic multiregional cortical coherence at multiple frequencies during visual task performance. Nature 1993;366:153–6.

Bressler SL, Large-scale cortical networks and cognition. Brain Res Rev 1995;20:288–304.

Burle B, Bonnet M. High-speed memory scanning: a behavioral argument for a serial oscillatory model. Cogn Brain Res 2000;9:327–37.

David O, Friston KJ. A neural mass model for MEG/EEG coupling and neuronal dynamics. NeuroImage 2003;20:1743–55.

David O, Cosmelli D, Lachaux JP, Baillet S, Garnero L, Martinerie J. A theoretical and experimental introduction to the non-invasive study of large-scale neural phase synchronization in human beings (invited paper). Int J Comput Cogn 2003;1(4):53–77.

David O, Cosmelli D, Friston KJ. Evaluation of different measures of functional connectivity using a neural mass model. NeuroImage 2004;21:659–73.

David O, Kilner JM, Friston KJ. Mechanisms of evoked and induced responses in MEG/EEG. NeuroImage 2006;31:1580–91.

Fisher NI. Statistical analysis of circular data. Cambridge University Press; 1995.

Friston KJ, Stephan KM, Frackowiak RSJ. Transient phase-locking and dynamic correlations: are they the same thing? Hum Brain Mapp 1997;5:48–57.

Gabor D. Theory of communication. Proc Inst Electr Eng 1946;93:429–41.

Gardner WA. A unifying view of coherence in signal processing. Signal Process 1992;29:113–40 (Elsevier).

Gevins A, Smith M, McEvoy L, Yu D. High-resolution EEG mapping of cortical activation related to working memory: effects of task difficulty, type of processing, and practice. Cereb Cortex 1997;7:374–85.

Gross J, Kujala J, Hämäläinen M, Timmermann L, Schnitzler A, Salmelin R. Dynamic imaging of coherent sources: Studying neural interactions in the human brain. PNAS 2001;98(2):694–9.

Guerrero JA, Marroquin JL, Rivera M, Quiroga JA. Adaptive monogenic filtering and normalization of ESPI fringe patterns. Opt Lett 2005;30(22):3018–20.

Haalman I, Vaadia E. Dynamics of neuronal interactions: relation to behavior, firing rates, and distance between neurons. Hum Brain Mapp 1998;5(4):249–53.

Harmony T, Fernandez T, Fernandez-Bouzas A, Silva-Pereyra J, Bosch J, Diaz-Comas L, et al. EEG changes during word and figure categorization. Clin Neurophys 2001;112:1486–98.

Harmony T, Fernandez T, Gersenowies J, Galan L, Fernandez-Bouzas A, Aubert E, et al. Specific EEG frequencies signal general common cognitive processes as well as specific task processes in man. Int J Psychophysiol 2004;53:207–16.

Hebb DO. The organization of behaviour. New York: Wiley; 1949.

Jensen O, Idiart MA, Lisman JE. Physiologically realistic formation of autoassociative memory in networks with theta/gamma oscillations: role of fast NMDA channels. Learn Mem 1996;3:243–56.

Junghöfer M, Elbert T, Tucker DM, Braun C. The polar average reference effect: a bias in estimating the head surface integral in EEG recording. Clin Neurophysiol 1999;10(6):1149–55.

Kirschfeld K. The physical basis of alpha waves in the electroencephalogram and the origin of the "Berger effect". Biol Cybern 2005;92:177–85.

Klimesch W. EEG alpha and theta oscillations reflect cognitive and memory performance: a review and analysis. Brain Res Rev 1999;29:169–95.

Klimesch W, Schack B, Schabus M, Doppelmayr M, Gruber W, Sauseng P. Phase-locked alpha and theta oscillations generate the P1-N1 complex and are related to memory performance. Cogn Brain Res 2004;19:302–16.

Lachaux JP, Rodriguez E, Martinerie J, Varela FJ. Measuring phase synchrony in brain signals. Hum Brain Mapp 1999;8:194–208.

Lachaux JP, Rodriguez E, Le Van Quyen M, Martinerie J, Varela FJ. Studying single-trials of phase-synchronous activity in the brain. Int J Bifur Chaos 2000;10:2429–39.

Law SK, Nunez PL, Wijesinghe RS. High-resolution EEG using spline generated surface Laplacians on spherical and ellipsoidal surfaces. IEEE Trans Biomed Eng 1993;40(2):145–53.

Lopes da Silva FH. Neural mechanisms underlying brain waves: from neural membranes to networks. Electroencephalogr Clin Neurophysiol 1991;79:81–93.

Marroquin JL, Mitter S, Poggio T. Probabilistic solution of ill-posed problems in computational vision. J Am Stat Assoc 1987;82:76–89.

Marroquin JL, Figueroa JE. Robust quadrature filters. J Opt Soc Am 1997;14(4):779–91.

Marroquin JL, Velasco FA, Rivera M, Nakamura M. Gauss-Markov measure field models for low-level vision. IEEE Trans Pattern Anal Mach Int 2001;23(4):337–48.

Marroquin JL, Harmony T, Rodriguez V, Valdes P. Exploratory EEG data analysis for psychophysiological experiments. NeuroImage 2004;21: 991–9.

Mizuhara H, Wang L, Kobayashi K, Yamaguchi Y. Long-range EEG phase synchronization during an arithmetic task indexes a coherent cortical network simultaneously measured by fMRI. NeuroImage 2005;27(3): 553–63.

Morecraft RJ, Geula C, Mesulam MM. Architecture of connectivity within a cingulo-fronto-parietal neurocognitive network for directed attention. Arch Neurol 1993;50(3):279–84.

Nunez PL. Neocortical dynamics and human EEG rhythms. Oxford University Press; 1995.

Nunez PL, Srinivasan R, Westdorp AF, Wijesinghe RS, Tucker DM, Silberstein RB, et al. EEG coherency I: statistics, reference electrode, volume conduction, Laplacians, cortical imaging, and interpretation at multiple scales. Electroencephalogr Clin Neurophysiol 1997;103:499–515.

Nunez PL. Toward a quantitative description of large-scale neocortical dynamic function and EEG. Behav Brain Sci 2000;23:371–437.

Perrin F, Pernier J, Bertrand O, Echallier JF. Spherical splines for scalp potential and current density mapping. Electroencephalogr Clin Neurophysiol 1989;72:184–7.

Perrin F, Pernier J, Bertrand O, Echallier JF. Corrigenda: EEG 02274. Electroencephalogr Clin Neurophysiol 1990;76:565.

Pfurtscheller G. Graphical display and statistical evaluation of event-related desynchronization (ERD). Electroencephalogr Clin Neurophysiol 1977;43:757–60.

Pfurtscheller G. Event-related synchronization: an electrophysiological correlate of cortical areas at rest. Electroencephalogr Clin Neurophysiol 1992;83:62–9.

Pfurtscheller G, Lopes da Silva FH. Event-related EEG/MEG synchronization and desynchronization: basic principles. Clin Neurophysiol 1999;110:1842–57.

Quian Quiroga R, Kraskov A, Kreuz T, Grassberger P. Performance of different synchronization measures in real data: a case study on electroencephalographic signals. Phys Rev E 2002;65:041903.

Quintana J, Fuster JM. From perception to action: temporal integrative functions of prefrontal and parietal neurons. Cereb Cortex 1999;9:213–21.

Rhom D, Klimesch W, Haider H, Doppelmayr M. The role of theta and alpha oscillations for language comprehension in the human electroencephalogram. Neurosci Lett 2001;310:137–40.

Rodriguez E, George N, Lachaux JP, Martinerie J, Renault B, Varela FJ. Perception's shadow: long-distance synchronization of human brain activity. Nature 1999;397:430–3.

Sarnthein J, Petsche H, Rappelsberger P, Shaw GL, Von Stein A. Synchronization between prefrontal and posterior association cortex during human working memory. Proc Natl Acad Sci USA 1998;95:7092–96.

Silverman BW. Density estimation for statistics and data analysis. London: Chapman and Hall; 1986.

Singer W. Synchronization of cortical activity and its putative role in information processing and learning. Ann Rev Physiol 1993;55:349–74.

Tallon-Baudry C, Bertrand O, Delpuech C, Pernier J. Oscillatory g-band (30–70 Hz) activity induced by a visual task in humans. J Neuroscience 1997;15:722–34.

Tallon-Baudry C, Bertrand O, Fisher C. Oscillatory synchrony between human extrastriate areas during visual short-term memory maintenance. J Neurosci 2001;15:RC177.

Ungerleider LG, Courtney SM, Haxby JV. A neural system for human visual working memory. Proc Natl Acad Sci USA 1998;95:883–90.

Varela FJ, Lachaux JP, Rodriguez E, Martinerie J. The brainweb: phase synchronization and large-scale integration. Nat Rev Neurosci 2001;2: 229–39.